ADVANCED FUNCTIONAL MATERIALS
www.afm-journal.de

www.MaterialsViews.com

Multifunctional Graphene Oxide-based Triple Stimuli-Responsive Nanotheranostics

Yu Chen, Pengfei Xu, Zhu Shu, Meiying Wu, Lianzhou Wang, Shengjian Zhang, Yuanyi Zheng, Hangrong Chen, Jin Wang, Yaping Li,* and Jianlin Shi**

Construction of multifunctional stimuli-responsive nanosystems intelligently responsive to inner physiological and/or external irradiations based on nanobiotechnology can enable the on-demand drug release and improved diagnostic imaging to mitigate the side-effects of anticancer drugs and enhance the diagnostic/therapeutic outcome simultaneously. Here, a triple-functional stimuli-responsive nanosystem based on the co-integration of superparamagnetic Fe_3O_4 and paramagnetic MnO_x nanoparticles (NPs) onto exfoliated graphene oxide (GO) nanosheets by a novel and efficient double redox strategy (DRS) is reported. Aromatic anticancer drug molecules can interact with GO nanosheets through supramolecular π stacking to achieve high drug loading capacity and pH-responsive drug releasing performance. The integrated MnO_x NPs can disintegrate in mild acidic and reduction environment to realize the highly efficient pH-responsive and reduction-triggered T_1-weighted magnetic resonance imaging (MRI). Superparamagnetic Fe_3O_4 NPs can not only function as the T_2-weighted contrast agents for MRI, but also response to the external magnetic field for magnetic hyperthermia against cancer. Importantly, the constructed biocompatible GO-based nanoplatform can inhibit the metastasis of cancer cells by downregulating the expression of metastasis-related proteins, and anticancer drug-loaded carrier can significantly reverse the multidrug resistance (MDR) of cancer cells.

1. Introduction

Combination of nanotechnology with biology, pharmacy and medicine can accomplish two critical clinical goals of oncology: precisely diagnosing the cancer at its early stage and effectively treating it upon positioning and identifying it.[1] Engineering of multifunctional nanosystems with stimuli-responsive performances has been demonstrated as a highly desirable strategy for the successful cancer treatment.[2] On the one hand, stimuli-responsive drug delivery systems (DDSs) can realize the on-demand drug release triggered by inner physiological changes (pH, redox, enzyme, competitive binding, etc.) and/or external irradiations (light, magnetic, electronic field, ultrasound, etc.), thus the side-effects caused by toxic drugs to normal tissues can be effectively mitigated and the therapeutic efficacy against cancer cells can be significantly enhanced.[3] On the other hand, stimuli-enhanced diagnostic imaging, such as magnetic resonance imaging (MRI), ultrasonography, fluorescence, and so on, can effectively improve the imaging performances of contrast agents (CAs) for accurate tumor imaging and detection.[4] However, the construction of multifunctional nanosystems with concurrent multiple stimuli-responsive drug release and diagnostic imaging still remains a great technical challenge though it is of substantial significance for realizing the simultaneous diagnostic imaging and therapy (designated as theranostic) for successful cancer treatments.

Exfoliated graphene oxide (GO) nanosheets, a parent material of graphene with unique free-standing two-dimensional crystallized structure and one-atom thickness, has been extensively explored in drug delivery,[5] gene transportation,[6] molecular imaging,[7] biosensing[8] and photothermal/photodynamic therapy,[9] mainly due to its high biocompatibility and unique physical/chemical properties such as excellent aqueous processability, abundant surface chemistry, near-infrared light

Dr. Y. Chen, Dr. Z. Shu, Dr. M. Wu, Prof. H. Chen, Dr. J. Wang, Prof. J. Shi
State Laboratory of High Performance Ceramic
and Superfine Microstructure
Shanghai Institute of Ceramics
Chinese Academy of Sciences
Shanghai 200050, P. R. China
E-mail: hrchen@mail.sic.ac.cn; jlshi@mail.sic.ac.cn
Dr. P. Xu, Prof. Y. Li
Shanghai Institute of Materia Medica
Chinese Academy of Sciences
Shanghai 201203, P. R. China
E-mail: ypli@mail.shcnc.ac.cn
Prof. L. Wang
ARC Centre of Excellence for Functional Nanomaterials
School of Chemical Engineering and AIBN
University of Queensland
St Lucia, Queensland, 4072, Australia
Dr. S. Zhang
Department of Radiology
Shanghai Cancer Hospital
Fudan University
Shanghai 200032, P. R. China
Prof. Y. Zheng
Second Affiliated Hospital of Chongqing Medical University
Chongqing, 400010, P. R. China

DOI: 10.1002/adfm.201400221

absorption, and so forth. In addition, GO also provides an excellent platform to be manipulated to accommodate different environment conditions, that is, for stimuli responsiveness-based biomedical engineering based on its carbonaceous composition and molecular structures.

Herein, we design an innovative class of GO-based multifunctional nanosystem for simultaneous triple stimuli-responsivenesses for biomedical engineering. Metal oxide composites including superparamagnetic iron oxide (Fe_3O_4) and paramagnetic manganese oxide (MnO_x) have been progressively loaded onto exfoliated GO nanosheets (designated as FeMn-GO) by a facile two-step double redox strategy (DRS), which elaborately utilizes the surface redox potential changes of GO. The resultant nanocomposites are expected to have the following four-fold functions: firstly, the GO nanosheets can interact with aromatic drug molecules through supramolecular π stacking, suggesting that the high drug loading capacity and controlled drug releasing performance might be achieved. Secondly, a special activatable MRI performance can be realized based on the disintegrating behavior of loaded MnO_x NPs under either mild pH environment or redox potential variations. The longitudinal r_1 can be significantly improved upon such stimuli changes. It is noted that the superparamagnetic Fe_3O_4 NPs act as the T_2-weighted MRI contrast agents (CAs), thus, FeMn-GO can perform as both the T_1- and T_2-weighted MRI CAs. Thirdly, the superparamagnetic FeMn-GO can be utilized for magnetic hyperthermia irradiated by external magnetic field, and the high heat transfer ability/thermal conductivity of GO synergistically improve the magnetic hyperthermia property owing to the loaded Fe_3O_4 NPs. Finally, FeMn-GO can inhibit the metastasis of cancer cells by downregulating the expression of metastasis-related proteins, and anticancer drug-loaded FeMn-GO can significantly reverse the multidrug resistance (MDR) of cancer cells.

2. Results and Discussion

2.1. Design, Synthesis, and Characterization of FeMn-GO

GO is highly hydrophilic due to the presence of large amounts of oxygen-containing groups, such as hydroxyl, epoxy, carbonyl, and so forth. (**Figure 1**a). These oxygen-containing groups offer

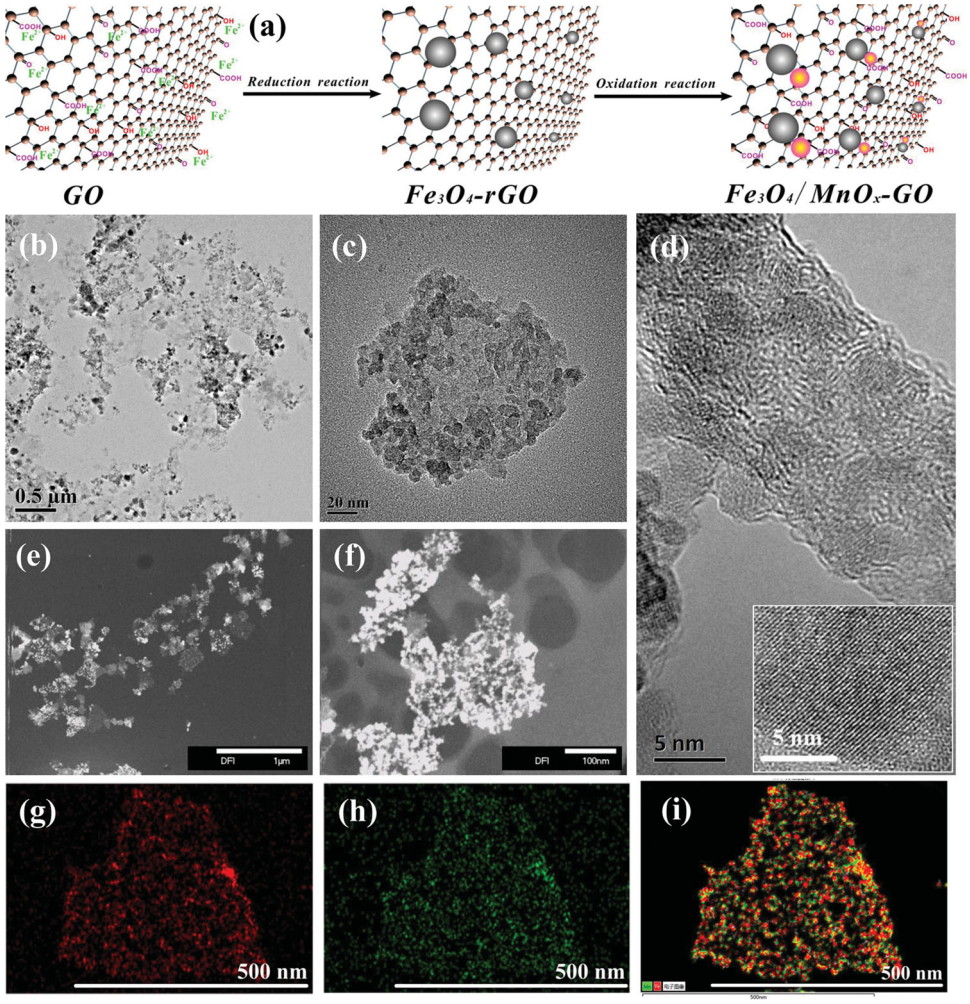

Figure 1. Design, synthesis and structural characterizations of FeMn-GO. a) Schematic illustration of double redox strategy (DRS) to synthesize FeMn-GO. b,c) TEM, d) HRTEM (inset: HRTEM image of Fe_3O_4 NPs), and e,f) dark field TEM images of FeMn-GO. Element mappings of g) Fe, h) Mn, and i) the merged image of (g,h).

the anchoring points for metal and/or metal oxides towards multifunctionalization. Especially, these oxygen-containing groups possess oxidizing potentials. They can oxidize Fe^{2+} in $FeSO_4$ to in-situ generate superparamagnetic Fe_3O_4 NPs binding on the GO's surface.[10] In the meantime, GO can be self-reduced by such redox process, and can be further oxidized by the introduction of $KMnO_4$. $KMnO_4$ can be in-situ reduced to produce MnO_x NPs by the second redox process. In this respect, GO acts as the oxidizing agent in the first redox step but as the reducing agent in the following second redox process. TEM images (Figure 1b,c) visualize large amount of NPs on the surface of GO, and the HRTEM (Figure 1d) image directly shows the crystal lattice of both Fe_3O_4 NPs and GO. The 0.29 nm lattice spacing in inset of Figure 1d is attributed to (100) phase of Fe_3O_4 NPs. The presence of composite MnO_x and Fe_3O_4 NPs can also be distinguished in dark field TEM (Figure 1e,f), SEM and EDS (Figure S1, Supporting Information). EDS element mapping (Figure 1i) shows that the Mn signal (Figure 1h) almost coincides with Fe signal (Figure 1g), which further evidences the synthetic mechanism that the introduction of Fe_3O_4 and MnO_x are mainly based on the changes of redox potential at the same active sites on GO (Figure 1a).

The prepared FeMn-GO can be well-dispersed in water with an average hydrated diameter of 215 nm determined by dynamic light scattering (DLS, Figure S2a and inset) measurement, as compared with a hydrated diamter of 342 nm in saline solution (Figure S2b, Supporting Information), indicating a little lowered stability. The magnetization curve of FeMn-GO (Figure S2c, Supporting Information) at 300 K shows the typical superparamagnetic characteristic nature with a saturation magnetization of 17.0 emu g^{-1}. The XRD pattern (Figure S2d, Supporting Information) shows a strong peak at $2\theta = 10.74°$ representing the feature diffraction peak of exfoliated GO.[11] After loaded with Fe_3O_4, the self-reduced GO shows the characteristic peak at $2\theta = 26.96°$ rather than at 10.74°. The representative peaks at $2\theta = 30.36°$, 35.42°, 43.27°, 57.43°, and 62.78° can be attributed to the (220), (311), (400), (511), and (440) crystal planes of cubic Fe_3O_4, respectively. It is noted that the characteristic peaks for MnO_x NPs in FeMn-GO are absent, suggesting that the formed MnO_x NPs are amorphous. XPS analysis of Fe 2p (Figure S2e, Supporting Information) and Mn 2p (Figure S2f, Supporting Information) was conducted on FeMn-GO to reveal the valence status of Fe and Mn. The peak fitting for Fe $2p_{3/2}$ shows two characteristic peaks at about 710 eV and 712 eV, respectively corresponding to Fe^{2+} and Fe^{3+}, and their ratio is about 1:2, indicating that the formed NPs are magnetic Fe_3O_4. The Mn $2P_{3/2}$ spectrum can be separated into three characteristic peaks located at about 641 eV, 642 eV, and 644 eV corresponding to Mn^{2+}, Mn^{3+}, and Mn^{4+}, respectively. The characteristic peaks of C 1s (Figure S2g, Supporting Information) at 285.7 eV and 287.6 eV are corresponding to the surface-adsorbed C-OH and their oxidation forms (e.g., epoxide), and carbon in association with oxygen in the carbonate ions, which contributes to the high hydrophilicity of FeMn-GO. The presence of Fe_3O_4 and MnO_x and their amounts in FeMn-GO can be further demonstrated and determined by FTIR (Figure S3, Supporting Information) and TG-DTA (Figure S4, Supporting Information) characterizations.

2.2. pH-Responsive T_1-Weighted MR Imaging

Due to the up-regulated glycolytic metabolism to generate the lactic acid, the tumorigenesis will give rise to more acidic microenvironment in tumors than in normal tissues, which provides the foundation for the construction of smart nanotheranostic agents sensitive to pH variations. The MnO_x NPs are very sensitive to such a mild acidity to disintegrate and produce Mn^{2+} ions, thus the interaction probability between paramagnetic centers and water molecules will be maximized, leading to the highly improved MRI-T_1 performance (**Figure 2**a). It is also noted that the manganese-based MRI-T_1 CAs are more biocompatible than cytotoxic Gd^{III}-based agents, as the US Food and Drug Administration (FDA) has warned that Gd element is associated with nephrogenic systemic fibrosis with impaired kidney function, but manganese element is the necessary element for physiological metabolism and the biological systems can control its homeostasis efficiently.[12] In this respect, the loaded MnO_x in FeMn-GO can act as the pH-activatable CAs for T_1-weighted MR imaging, and the remaining Fe_3O_4 NPs can function as the efficient MRI-T_2 CAs after MnO_x disintegration.

The in vitro dynamic disintegrating of MnO_x NPs to release Mn^{2+} by responding to the mild pH changes and the resultant simultaneous enhancement of MRI-T_1 performances were directly evaluated in a 3 T clinical MRI apparatus by immersing FeMn-GO NPs in the buffer solution with pH values of 7.4 and 6.0 (Figure 2b and Supporting Information Figure S5), which were chosen to imitate the normal blood circulation and tumor acidic environment, respectively. The apparent MRI-T_1 signal enhancement initially takes place in the very small region in buffer solution with pH = 6.0, then becomes prevailing rapidly accompanying the fast releasing of Mn^{2+}. Very strong positive MRI-T_1 signal enhancement can be found in the whole buffer solution in a short time period (45 min). Comparatively, FeMn-GO soaking in the neutral buffer solution exhibits almost no significant signal variations. It is noted that the negative MRI-T_2 signal can also be enhanced by decreasing pH value. The MRI-T_1 (Figure 2c) and MRI-T_2 (Figure 2d) signal variations corresponding to varied Mn and Fe concentrations further demonstrate such a pH-responsiveness. The relaxation rate r_1 (Figure 2e) of FeMn-GO corresponding to Mn concentration variation substantially increases from 1.2 $mM^{-1}s^{-1}$ to 5.6 $mM^{-1}s^{-1}$ accompanying the decrease of pH from 7.4 to 6.0, nearly 4-fold magnitude increase. This r_1 value is also much higher than that of commercial Gd-based CAs ($r_1 \approx 3.4$ $mM^{-1}s^{-1}$) and nearly 10-fold magnitude to MnO_x NPs with varied particle sizes (typically smaller than 0.5 $mM^{-1}s^{-1}$).[13] Comparatively, the relaxation rate r_2 (Figure 2f) corresponding to Fe concentration variation increases significantly from 65.9 $mM^{-1}s^{-1}$ to 103.17 $mM^{-1}s^{-1}$. Such an increase in MRI-T_2 performance was due to the contribution from the released manganese ions, which result in more darkened T_2-weighted MRI images.[4a] Therefore, FeMn-GO can be used as both the pH-responsive T_1- and T_2-wieghted MRI CAs. The STEM image and element mapping of FeMn-GO after 4 h soaking in pH = 6.0 buffer solution (Figures S6,S7, Supporting Information) show that the dispersity and lamellar morphology of FeMn-GO can still be maintained but the Mn element cannot be detected after the soaking, further indicating the disintegrating behavior of MnO_x NPs from FeMn-GO. It is noted that the enhanced T_1-weighted MRI performances

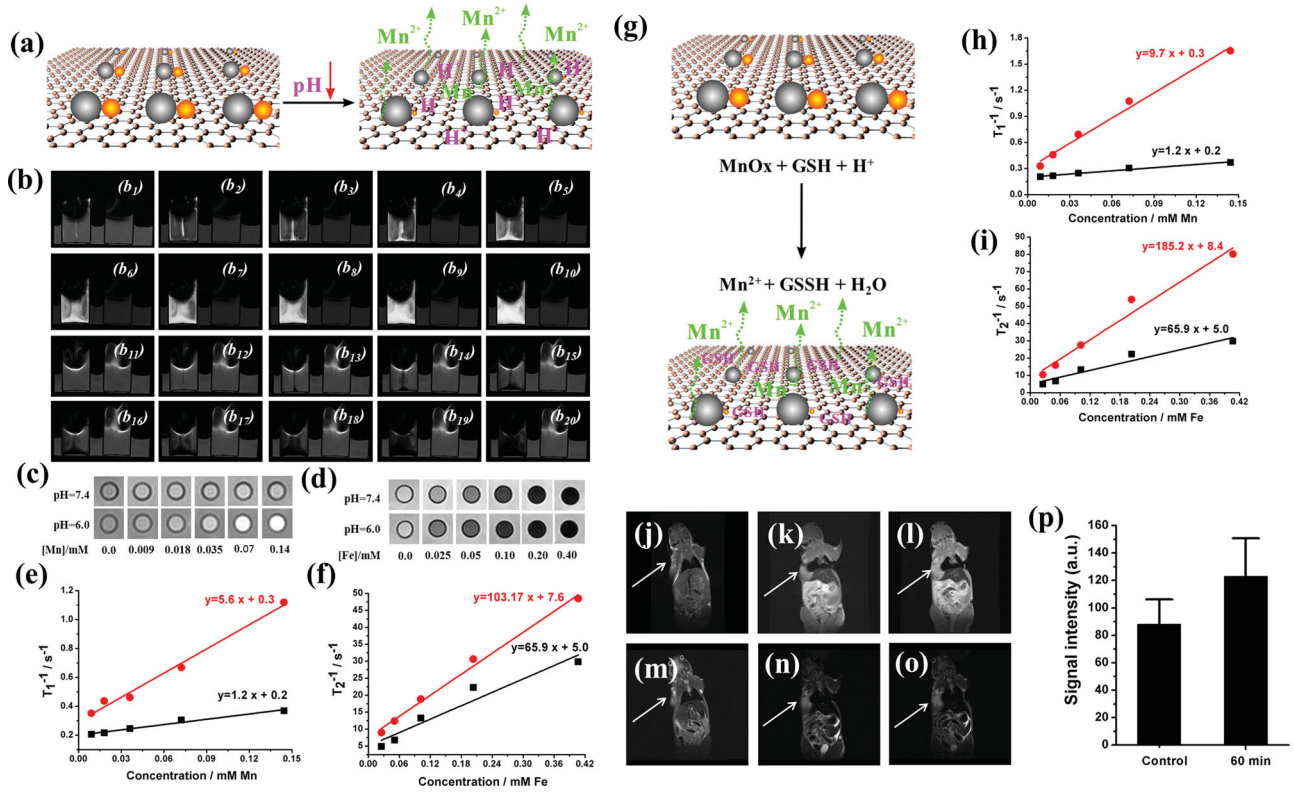

Figure 2. pH- and reduction-responsive T_1-weighted MRI. a) Schematic illustration of co-loading of Fe_3O_4 and MnO_x on GO and the disintegrating of MnO_x in mild acidic environment. b) In vitro dynamic measurement of T_1- (b_1-b_{10}) and T_2-weighted (b_{11}-b_{20}) MRI of FeMn-GO in the buffer solution with different pH values (b_1 and b_{11}: 0 min, b_2 and b_{12}: 5 min, b_3 and b_{13}: 10 min, b_4 and b_{14}: 15 min, b_5 and b_{15}: 20 min, b_6 and b_{16}: 25 min, b_7 and b_{17}: 30 min, b_8 and b_{18}: 35 min, b_9 and b_{19}: 40 min, b_{10} and b_{20}: 45 min; in each photo, left: pH = 6.0; right: pH = 7.4;). c) T_1- and d) T_2-weighted solution MRI of FeMn-GO in buffer solution at different pH values after soaking at 37 °C for 4 h. e) T_1 and f) T_2 relaxivity of the buffer suspension of FeMn-GO after 4 h soaking under different pH values (black line: 7.4 and red line: 6.0) at 37 °C. g) Schematic illustration of Mn^{2+}release upon the change of redox environment. h) T_1 and i) T_2 relaxivity of the buffer suspension of FeMn-GO after 4 h soaking under different redox environment at 37 °C (black line: 0 mM and red line: 1.0 mM GSH). j–l) T_1- and m–o) T_2-weighted in vivo tumor imaging j,m) before and k,l,n,o) after (k and n: 30 min, l and o: 60 min) intravenous administration of FeMn-GO. p) The relative T_1-weighted positive MRI signal intensity of tumor before and after 60 min administration of FeMn-GO.

triggered by either pH or redox environment variations can significantly reduce doses of CAs to achieve the desired imaging results. Thus, the toxicity of manganese can be significantly mitigated.

2.3. Reduction-Responsive T_1-Weighted MR Imaging

It has been demonstrated that glutathione (GSH) is a common reducing agent within cancer cells, and the GSH levels in human cancer tissues are significantly higher than the normal tissue.[14] MnO_x NPs within FeMn-GO are highly susceptible to such a redox environment. They can easily disintegrate into Mn^{2+} by reducing Mn (III) and Mn (IV) into Mn (II) in the reducing environment, and GSH can be oxidized into oxidized glutathione (GSSG, Figure 2g). Such a reduction-induced dissolution of paramagnetic MnO_x can be directly demonstrated by the changes of relaxation rate r_1 and r_2. The r_1 (Figure 2h) can reach 9.7 mM^{-1} s^{-1} after the co-incubation in 1.0 mM GSH solution for 4 h, substantially higher than commercial Gd-based CAs and nearly 90-fold magnitude that of traditional MnO NPs.[13] Importantly, the relaxation rate r_2 (Figure 2i) corresponding to Fe concentrations increases significantly from 65.9 $mM^{-1}s^{-1}$ to 185.2 $mM^{-1}s^{-1}$. In this respect, FeMn-GO can act as both the redox-responsive T_1- and T_2-wieghted MRI CAs with high relaxivity rates.

To demonstrate the pH-/redox-responsive in vivo tumor imaging capability of FeMn-GO, we established a 4T1 breast cancer xenograft in nude mice by subcutaneous injection of 1×10^6 4T1 cells suspended in 50 µL sterile PBS for the in vivo MRI evaluation. As shown in Figure 2j–l, the FeMn-GO exhibits the strong T_1-weighted positive contrast-enhanced MR imaging of tumor tissues in 30 min of post-intravenous administration (Figure 2k), and the signal intensity increases in the time course of injection (60 min, Figure 2l,p). Interestingly, the liver shows strong enhancements of negative signals both in T_1- and T_2-weighted MR images (Figure 2j-o). This can be attributed to the strong negative effect caused by the superparamagnetic Fe_3O_4 NPs within FeMn-GO for efficient MRI-T_2, which shields and disables the positive effect of MnO_x for MRI-T_1. However, when FeMn-GO researches the tumor tissue via the typical enhanced permeability and retention (EPR) effect, MnO_x NPs will disintegrate under the specific triggers of both acidic and reducing environment, thus the tumor tissues can be imaged in T_1-

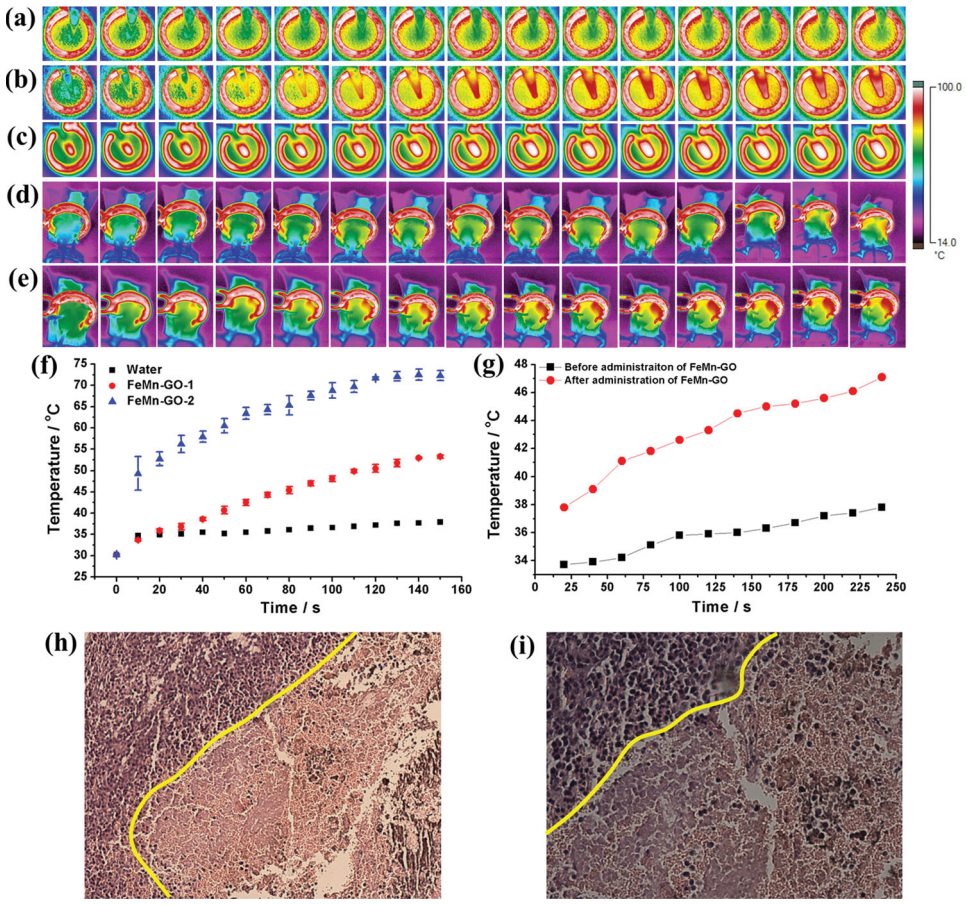

Figure 3. In vitro and in vivo magnetothermal property of FeMn-GO. In vitro thermal images of a) aqueous solutions and FeMn-GO aqueous solutions at Fe concentrations of b) 3.25 mM and c) 6.5 mM. In vivo thermal images of mice d) before and e) after administration of FeMn-GO and g) their corresponding quantitative temperature-time curve under magnetic field. f) Quantitative temperature-time curve of water and FeMn-GO aqueous solution under magnetic field. Microscopic images of tumor sections after magnetic hyperthermia under the assistance of FeMn-GO at different magnifications: h) 100× and i) 200×. These in vitro and in vivo images were recorded every 10 s and 20 s, respectively, under an alternative magnetic field (power = 6 kW, frequency f = 600 kHz and coil diameter = 3 cm).

weighted MRI due to the release and diffusion of Mn^{2+}. Thus Fe_3O_4 NPs will have negligible influence on MRI-T_1 capability of released Mn^{2+} because of the diffusion-off of Mn^{2+} from FeMn-GO. In addition, the strong T_1- and T_2-weighted kidney MR imaging further demonstrates the release of Mn^{2+} (Figure S8, Supporting Information). It is generally accepted that only NPs with the particle size of less than 5.5 nm can be cleared through the kidney.[15] Apparently, the particle size of FeMn-GO is larger than this size limitation, therefore, the strong T_1-MRI signal intensity can be determined to be the effect of released Mn^{2+}.

2.4. Magnetic Field-Responsive Hyperthermia of Cancer

In addition to the loaded MnO_x for the responsive MRI-T_1, the integrated superparamagnetic Fe_3O_4 NPs can not only act as the CAs for T_2-weighted MRI but also exhibit the fast responsiveness to external alternating magnetic field, thus they can be directly used for magnetic hyperthermia treatment (MHC) of cancer. It is found that the temperature of FeMn-GO aqueous solution increases rapidly under the alternating magnetic field while the control water solution does not exhibit such an effect (**Figure 3**a–c,f). The temperatures can be raised to 72 °C and 53 °C after 150 s heating at the Fe concentrations of 6.5 mM and 3.25 mM. The in vivo magnetic hyperthermia potential of FeMn-GO was evaluated preliminarily by intratumor administration of FeMn-GO (200 µL per mouse, 6.5 mM). It is found that the skin surface temperature of tumor can be fast elevated to 47 °C in 240 s-magnetic heating (Figure 3e,g) while the control mouse without the administration of FeMn-GO exhibits only a slight temperature increase (Figure 3d,g, 37.8 °C after 240 s-heating), determined by thermal imaging analysis.

To further assess the magnetic hyperthermia efficacy against tumor tissues, hematoxylin and eosin (H&E) stain of tumor-sections after hyperthermia treatment was conducted. Large amounts of cell death caused by cell necrosis can be observed (Figure 3h,i) on the section following hyperthermia under the assistance of FeMn-GO. In addition, the boundary between necrosis and compact normal tissues can be clearly observed, also large vacuoles and irregular widening of tumor tissues can be found in the necrosis region. These thermal analysis and H&E results show that FeMn-GO can fast response to external magnetic field to induce the tumor cell necrosis and death by hyperthermia.

2.5. pH-Responsive Anticancer Drug Release

Anticancer drug, aromatic doxorubicin (DOX) molecules, can be easily loaded onto FeMn-GO by a simple mixing process with both high loading amount (380 mg g^{-1}) and efficiency (95%) demonstrated by the absence of typical absorption peak of DOX in UV-vis spectra after the loading process (Figure S9). Such a high loading amount and efficiency can be attributed to the unique non-covalent π–π stacking and hydrophobic interactions between multifunctional GO and aromatic DOX molecules (**Figure 4**a).[16] Importantly, such an interaction can be easily changed and regulated by external triggers such as acidity. The in vitro DOX-releasing profiles of DOX-loaded FeMn-GO were conducted under different pH conditions (pH = 7.4, 6.0, and 4.6). It can be found (Figure 4b) that the release of DOX from FeMn-GO is greatly inhibited in the neutral solution with only a 3.1% 24 h-releasing amount, but accelerated in mildly acidic buffer solution with 24 h-releasing amounts of 5.1% (pH. 6.0) and 11.2% (pH. 4.6), respectively. Upon changing the pH value from 7.4 to 4.6 and 6.0 to 4.6, the releasing rate of DOX from the carrier can be significantly accelerated, further demonstrating the fast pH-responsiveness. This pH-responsive behavior is very suitable for tumor chemotherapy: the release of DOX from FeMn-GO is extremely low when they circulate within the neutral blood vessel, while the releasing rate significantly increases upon accumulation within acidic tumor tissues. Thus, the toxic side-effects of DOX to normal tissues can be substantially mitigated and the corresponding therapeutic outcomes can be enhanced. The acidity-triggered DOX release from FeMn-GO is also accompanied by the simultaneous leaking of Mn^{2+} caused by the disintegrating of MnO_x NPs. The relaxation time T_1 (Figure 4c) and T_2 (Figure 4d) of 24 h-releasing buffer solution at low pH values (6.0 and 4.6) can be significantly shortened compared to the neutral solution

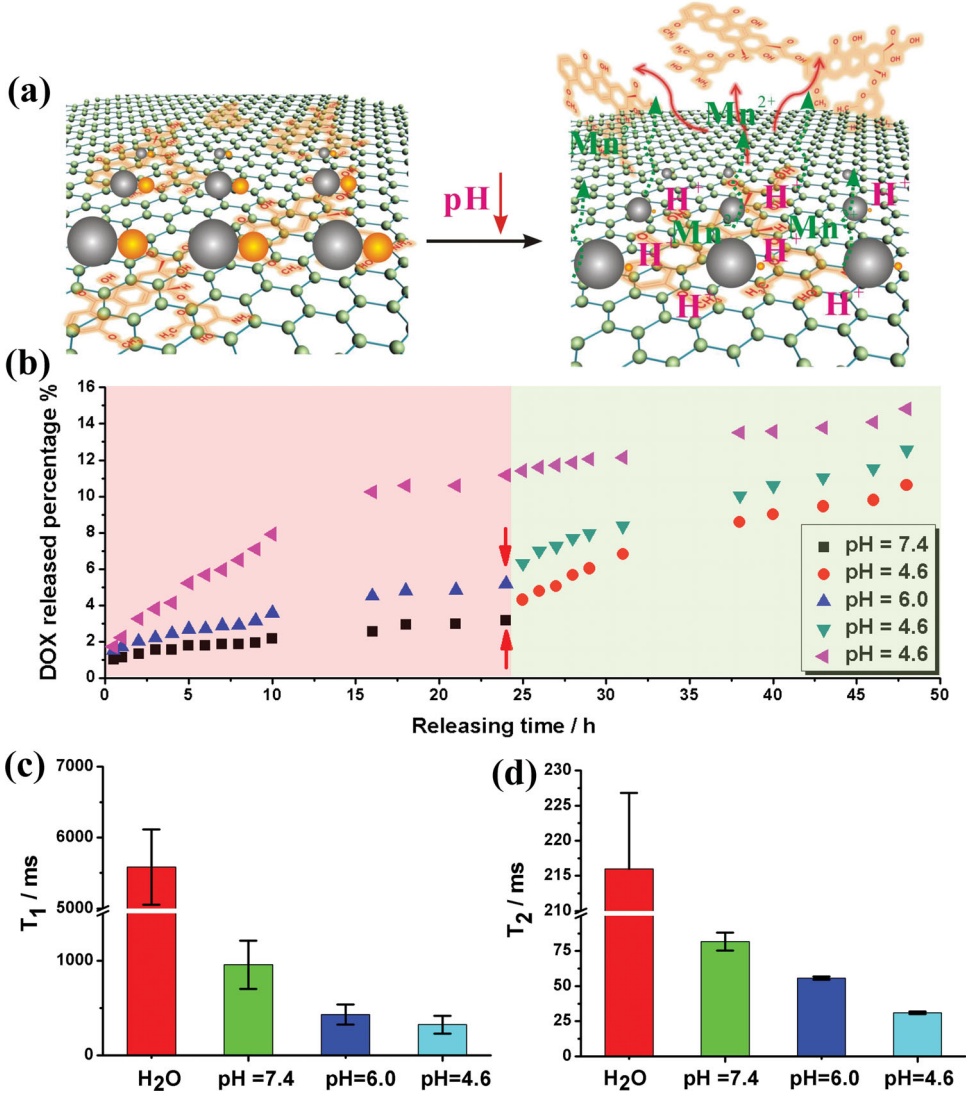

Figure 4. pH-responsive anticancer drug release. a) The scheme of molecular interaction between GO carbonaceous framework and aromatic DOX molecules via supramolecular π stacking, and the corresponding DOX release upon the decrease of pH. b) In vitro DOX release from DOX-loaded FeMn-GO in buffer solutions of varied pH values (7.4, 6.0, and 4.6). c) T_1 and d) T_2 values of 24 h DOX-releasing solution.

(pH. 7.4). Such a behavior can be potentially utilized for the in-situ observation and determination of the pH-responsive drug release via T_1- and T_2-weighted MRI during chemotherapy.

2.6. Antimetastasis and Reversing the MDR of Cancer Cells

GO has been extensively explored as the efficient DDSs for drug delivery and their high biocompatibility has been well demonstrated.[5,17] The fundamental issues regarding their biological effect on metastatic cells and multidrug resistant cancer cells, however, have not been reported so far. We further investigated the antimetastasis behaviors of FeMn-GO and their capability to reverse the MDR of cancer cells in detail. After the incubation of FeMn-GO with highly metastatic human breast cancer cell MDA-MB-231 at elevated concentrations, it is interesting to find that the migration capability of invasive MDA-MB-231 cells can be significantly inhibited (**Figure 5**a,e and Supporting Information Figure S10). To further imitate the in vivo metastasis environment, the MDA-MB-231 cells were seeded onto the surface of transwell chamber coated with a matrigel layer. The invasiveness of cancer cells (Figure 5b) can also be

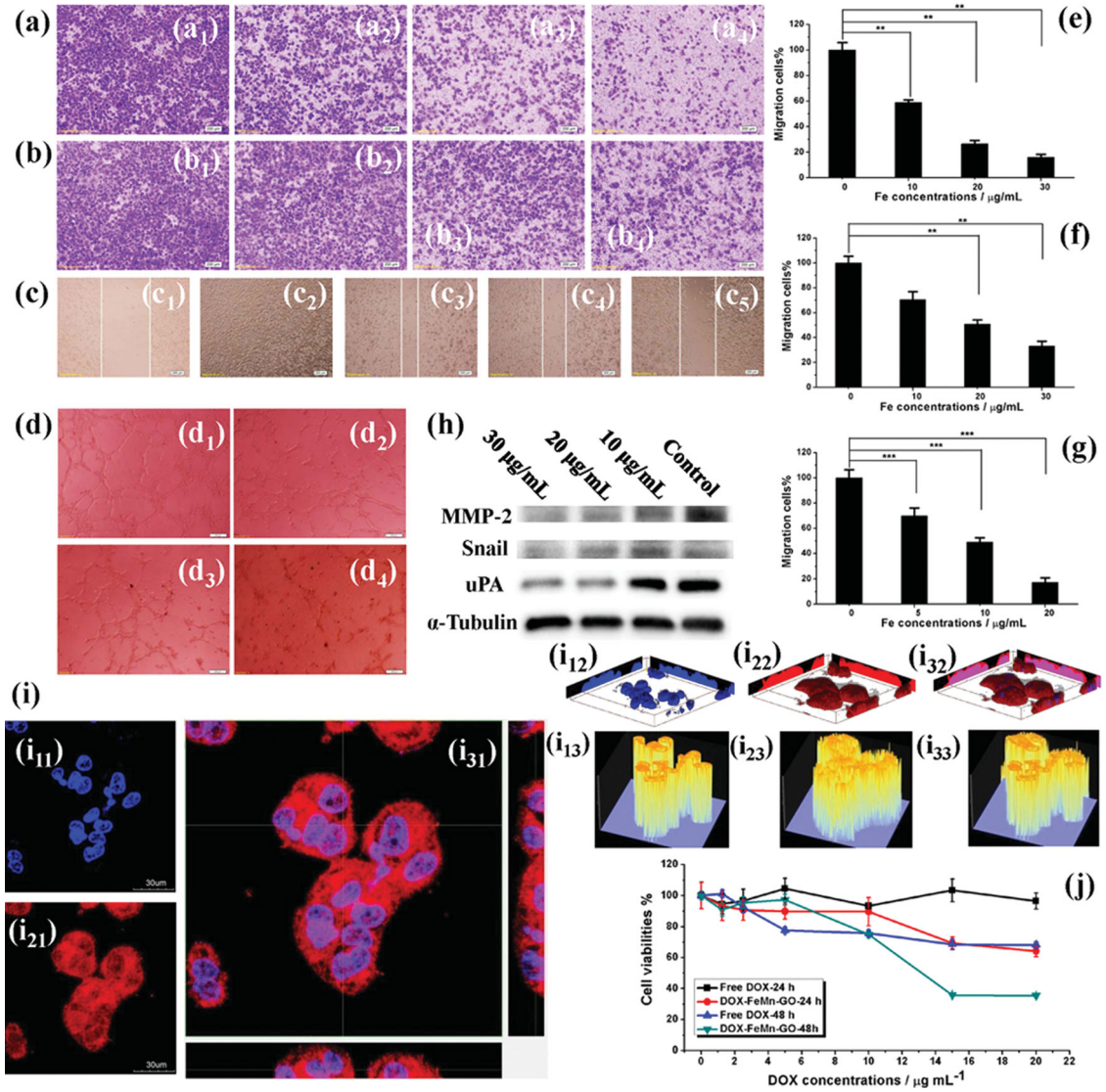

Figure 5. Antimetastasis and reversing the MDR of cancer cells mediated by FeMn-GO. a) Migrated and b) invasive MDA-MB-231 cancer cells after co-incubation with FeMn-GO of varied Fe concentrations (a_1 and b_1: control, a_2 and b_2: 10 μg mL^{-1}, a_3 and b_3: 20 μg mL^{-1}, a_4 and b_4: 30 μg mL^{-1}). c) Wound healing assay for the observation of migratory potential of MDA-MB-231 cells after co-incubation without (c_1) and after co-incubation with FeMn-GO of varied concentrations (c_2: 10 μg mL^{-1}, c_3: 20 μg mL^{-1}, c_4: 30 μg mL^{-1}). d) In vitro capillary tube formation after the treatments with FeMn-GO of different concentrations (d_1: control, d_2: 10 μg mL^{-1}, d_3: 20 μg mL^{-1}, d_4: 30 μg mL^{-1}). Quantitative results of e) migrated, f) invasive, and g) capillary tube formation percentages of per 200× field in microscopic images. h) Western-blotting analyses of the expressions of MMP-2, Snail, and uPA proteins of MDA-MB-231 cancer cells after co-incubation with FeMn-GO at elevated concentrations. i) CLSM images (i_{11}: nuclei, i_{21}: DOX, i_{31}: merged image of i_{11} and i_{21}; [DOX] = 10 μg mL^{-1}) of MCF-7/ADR cancer cells after co-incubation with DOX-loaded FeMn-GO, their corresponding 3D confocal fluorescence reconstructions (i_{12}: nuclei, i_{22}: DOX, i_{32}: merged image of i_{12} and i_{22}) and fluorescent intensities of cells in i_{31} (i_{13}: nuclei, i_{23}: DOX, i_{33}: merged image of i_{13} and i_{23}). j) Cell viabilities of MCF-7/ADR cells after co-incubation with DOX-loaded FeMn-GO ([DOX] = 10 μg mL^{-1}). Scale bars of (a–d) are 200 μm.

strongly inhibited with only 33% of the control group after the co-incubation with FeMn-GO of 30 μg mL^{-1} (Figure 5f). The evaluation of the reparation behavior of artificially wounded area shows that the migration of MDA-MB-231 cells to repair the wounded area can be strongly suppressed (Figure 5c), and this effect is also strongly dependent on the FeMn-GO concentrations. In addition to the capability of FeMn-GO to inhibit the migration and invasion of invasive MDA-MB-231 cancer cells, it can also inhibit the formation of capillary tubes and cellular network structure of human microvasuclar endothelial cells (HMEC) by a typical anti-angiogenesis assay (Figure 5d,g and Supporting Information Figure S11). These four representative in vitro assays provide the confident evidences for the further in vivo antimetastasis and anti-angiogenesis via the introduction of FeMn-GO. To further reveal the mechanism of such antimetastasis effects, the expression of main proteins related to the metastasis of MDA-MB-231 cancer cells were determined by typical western-blotting analysis (Figure 5h). It can be found that the expression of MMP-2, Snail and uPA has been significantly inhibited after the co-incubation with FeMn-GO with different concentrations,[18] which further manipulates the migration and invasive behaviors of the cancer cells. Recent theoretical models show that NPs inhibit matrix metalloproteinases *via* an exocite interaction, whereas the well-known zinc catalytic site only exerts a minimal role. Thus, the expression and activity of MMPs associated with metastasis of cancer cells could be significantly reduced.[19]

The intracellular drug delivery by DOX-encapsulated FeMn-GO was evaluated against DOX-resistance breast cancer cell MCF-7/ADR. From confocal laser scanning microscopy (CLSM) images, it can be found (Figure 5i_{11},i_{21},i_{31}) that a large amount of DOX molecules can be delivered within cancer cells mediated by FeMn-GO. Three-dimensional fluorescence reconstruction (Figure 5i_{12},i_{22},i_{32}) and the fluorescent intensity tests (Figure 5i_{13},i_{23},i_{33}) further demonstrate that DOX molecules are present within the whole cancer cells, and large amounts of them are present within the nuclei. Cell cytotoxicity (Figure 5j) tests reveal that free DOX exhibits low cytotoxicity against MCF-7/ADR cells due to the multidrug efflux pump effect by the over-expressed P-glycoprotein (P-gp),[20] which can pump DOX molecules from the cytoplasm out of cancer cells. Comparatively, DOX-loaded FeMn-GO shows the substantially higher cytotoxicities than free DOX because the P-gp-induced efflux process can be effectively bypassed via FeMn-GO due to the remarkably larger particle sizes of FeMn-GO compared to free DOX molecules.

3. Conclusion

In summary, a nanographene oxide-based multifunctional triple stimuli-responsive nanosystem has been constructed by a unique sequential double redox strategy (DRS) to co-integrate superparamagnetic Fe_3O_4 and paramagnetic MnO_x NPs on GO. These synthesized FeMn-GO NPs are highly biocompatible as demonstrated by the low cytotoxicity and high histocompatibility (Figures S12,13, Supporting Information). The whole cancer theranostic map based on FeMn-GO is illustrated in **Figure 6**. Hydrophilic FeMn-GO NPs can circulate within blood vessels due to their small particle size, and enter the tumor tissue via the typical enhanced permeability and retention (EPR) effect. The MnO_x NPs are shielded from neutral aqueous environment by surrounding Fe_3O_4 NPs, resulting in the minimized interaction probability with water molecules and quenched T_1-weighted MRI signal enhancement ("OFF" state). Upon triggered by acidic and/or redox environment of tumor tissues, Mn^{2+} will release from FeMn-GO by the disintegration of MnO_x NPs to generate a strong positive contrast enhancement ("ON" state, Figure 2). Such an efficient pH- and/or redox-responsive T_1-weighted MRI feature by Mn^{2+} ion release highly facilitates MRI and can be used to obtain the feedback of chemotherapy, which are the predominant stimuli during the diagnostic imaging process. Meanwhile, the integrated Fe_3O_4 NPs can not only act as the efficient MRI-T_2 CAs, they can also function as hyperthermia agents for magnetic-field induced tumor cell necrosis (Figure 3).

The endocytosis of FeMn-GO by cancer cells can significantly downregulate the expression of metastasis-related proteins (MMP2, Snail, uPA, etc.), leading to substantially inhibited migration and invasion of cancer cells (Figure 5a–h). The acidic tumor extracellular environment and organelles (e.g., endosomes and lysosomes: pH.5.0–5.5) can trigger the DOX-releasing (Figure 4a,b) from FeMn-GO to efficiently reverse the MDR of cancer cells (Figure 5i,j). The magnetic field-induced hyperthermia process can further improve the therapeutic outcome of cancer. Thus, the pH-triggered drug release and magnetic field-induced hyperthermia will be the predominant stimuli-responsive mechanisms during the therapeutic process. On this ground, the proof-of-concept design of GO-based triple stimuli-responsive nanosystem can be considered as a simple and cost-effective new approach to realize the theranostics of cancer in an intelligent, on-demand and efficient manner, which may pave the pathways towards new generation of nanobiotechnology.

4. Experimental Section

Materials: Graphene oxide was obtained from Nanjing XianFeng Nano Material Technology Co. Ltd (XFNANO), which was synthesized by a traditional Hummers' method. Potassium permanganate ($KMnO_4$), ferrous sulfate ($FeSO_4{\cdot}7H_2O$), ammonium hydroxide aqueous solution (NH_4OH, 25–28%) were obtained from Sinopharm Chemical Reagent Co. Anticancer agent doxorubicin hydrochloride (DOX·HCl) was purchased from Bejing Huafeng United Technology Co., Ltd. Phosphate buffer solution (PBS) was purchased from Shanghai Ruicheng Bio-Tech Co., Ltd. Trypsin-EDTA and fetal bovine serum (FBS) were purchased from Gibco-BRL (Burlington, Canada). Dulbecco's Modified Eagle's Medium (DMEM) and antibiotics were obtained from Invitrogen (Oregon, USA). Matrigel was bought from BD Biosciences (San Jose, USA). RIPA lysis buffer, Crystal Violet, hematoxylin and eosin were obtained from Beyotime Institute of Biotechnology (Haimen, China). All regents were used without further purification. Deionized water was used in all synthetic experiments.

Synthesis of FeMn-GO: GO was firstly dispersed into aqueous solution with the concentration of 1 mg/mL by ultrasonic (800 W) treatment for 8 h. This process can produce stable GO aqueous solution with small particle sizes. For Fe_3O_4 loading, ammonia solution (1 mL, 25%–28%) was added into GO solution (1 mg mL^{-1}, 10 mL) under magnetic stirring at room temperature. Then, the fresh prepared $FeSO_4{\cdot}7H_2O$ solution (0.5 M, 0.1 mL) was dropwise added into above GO solution,

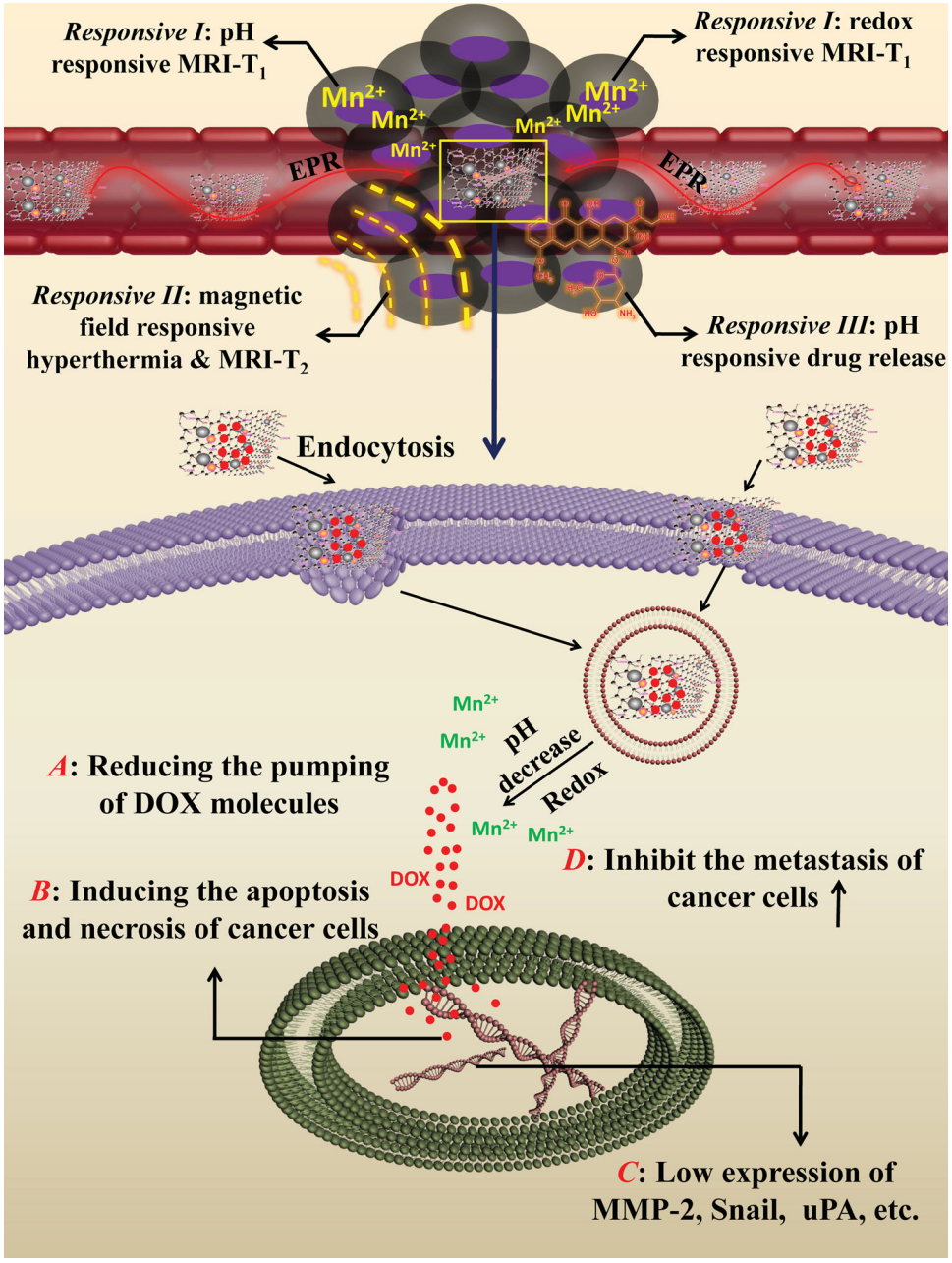

Figure 6. Schematic of FeMn-GO for biomedical engineering. Theranostic map of FeMn-GO with triple stimuli-responsivenesses for intelligent T_1-weighted MRI, magnetic hyperthermia, antimetastasis of cancer cells, intracellular anticancer drug delivery, and reversing the MDR of cancer cells.

and the reaction was continued for another 10 min. The product was collected by centrifugation, washed with water for three times and re-dispersed into aqueous solution (20 mL) by ultrasound treatment. Then, the fresh prepared $KMnO_4$ aqueous solution (0.05 M, 20 mL) was added into Fe_3O_4-GO dispersions dropwise under the magnetic stirring. The redox reaction was continued for another 4 h at room temperature under magnetic stirring in the dark. Finally, the prepared FeMn-GO was collected by centrifugation and washed with water for 6 times to remove unreacted MnO_4^-, which was further dispersed into aqueous solution for further use.

In Vitro and In Vivo MRI Assay: The in vitro and in vivo MR imaging experiments were performed on a 3.0 T clinical MRI instrument (GE Signa 3.0 T). For in vitro pH-responsive relaxation test, the manganese and iron concentrations of FeMn-GO dispersed in water were determined by inductively coupled plasma atomic emission spectrometry (ICP-AES). FeMn-GO was firstly dispersed into two buffer solution with different pH values: (PBS, pH = 7.4) and citrate acid-sodium citrate buffer solution (0.1 M, pH = 6.0). After the mild shaking at the speed of 100 rpm at 37 °C for 4 h, the FeMn-GO buffer solutions were diluted with corresponding xanthan gum buffer solution (≈0.1%) to obtain the desired concentrations. Finally, the FeMn-GO buffer solutions (1 mL) with different concentrations were transferred into Eppendorf tubes (1.5 mL) for MRI test. For in vitro reducing-responsive relaxation test, FeMn-GO was dispersed into GSH solution (1.0 mM) for 4 h incubation with shaking at the speed of 100 rpm at 37 °C. The following step is the same as the procedure for pH-responsive MRI-T_1 measurement. T_1-weighted Fast-recovery spin-echo (FR-FSE) sequence is described as follows: TR = 1000, 2000, 3000, and 4000, Slice = 3 mm,

Space = 0.5 mm, Fov = 20, Phase fov = 0.8, Freq × Phase = 384 × 256, Nex = 2, ETL = 2. For in-situ dynamic evaluation of Mn^{2+} leakage and MRI-T_1 signal enhancement, FeMn-GO aqueous solution (1 mL, 6.5 mM) was put in a dialysis bag (cutoff molecular weight: 5000), which was further impregnated into buffer solutions with different pH values (7.6 and 6.0, Figure S5, Supporting Information). The MRI-T_1 images were acquired at given time intervals. For in vivo MRI evaluation, the 4T1 orthotopic mammary tumor metastasis model was established by subcutaneous injection of 1×10^6 4T1 cells suspended in 50 μL sterile PBS into the mammary fat pad of female nude mouse. MRI assay was carried out after the tumor growth for two weeks. In vivo MRI was performed at selected time intervals before and after intravenous injection of FeMn-GO suspensions (dose: 2.5 mg Mn per kg of mouse body).

In Vitro and In Vivo Magnetic Hyperthermia Evaluations: For in vitro evaluation, FeMn-GO with different concentrations (0, 3.25 and 6.5 mM; 1mL) was added into Eppendorf tubes (1.5 mL), which was further put into the center of magnetic field. After different magnetic irradiation intervals, the thermal images of FeMn-GO dispersions were acquired by a thermal imaging camera to determine the temperature variations. For *in vivo* assay, the tumor-bearing mouse was intratumorly administrated with FeMn-GO solution ([Fe] = 6.5 mM, 200 μL), the thermal images before and after administration of FeMn-GO solution was acquired after different magnetic irradiation intervals.

Encapsulation of DOX onto FeMn-GO: FeMn-GO (freeze-dried sample, 15 mg) was dispersed into DOX PBS solution (20 mL, 0.5 mg mL^{-1}) by ultrasound treatment. Then, the co-incubation was continued for another 24 h in the dark at room temperature by magnetic stirring. The DOX-loaded FeMn-GO was collected by centrifugation and freeze-dried. The initial DOX solution and supernatant DOX solution after loading were analyzed by UV-vis test at λ = 480 nm. The loading efficiency of DOX in FeMn-GO was calculated as follows: $(W_{ini} - W_{res}) / W_{ini} \times 100\%$ (W_{ini}: initial amount of DOX, W_{res}: residual DOX amount). The DOX loading amount is calculated to be 380 mg/g, and the loading efficiency is nearly 95%.

In vitro DOX Releasing from DOX-loaded FeMn-GO in the Releasing Buffer Solution with Different pH Values (pH = 7.4, 6.0 and 4.6): DOX-loaded FeMn-GO (5 mg) were encapsulated into a dialysis bag (cutoff molecular weight: 5000) and put into the releasing buffer medium (25 mL) with different pH values (pH = 7.4, 6.0 and 4.6). Then, the dialysis bag was further put in a shaking table with the shaking speed of 100 rpm at 37 °C. At given time, 3 mL releasing solution was taken out for the measurement by UV-vis adsorption spectra at λ = 480 nm. Then, the tested releasing solution was further poured back into the initial releasing medium for further evaluation. After 24 h-releasing, the releasing medium at pH = 7.4 and 6.0 was replaced with solution at pH = 4.6 for further monitoring of the releasing profiles.

Cell Culture: The human mammary tumor cell line (MDA-MB-231) was cultured in DMEM (Dulbecco's Modified Eagle Medium, Gibco, USA) containing 10% fetal bovine serum (FBS), 100 U/mL penicillin G sodium, 100 μg mL^{-1} streptomycin sulfate and 2 mM L-glutamine. DOX-resistant breast cancer cell line (MCF-7/ADR) was culture in RPMI 1640 cell growth medium containing 1 μg/mL DOX, 10% fetal bovine serum (FBS), 100 U mL^{-1} penicillin G sodium and 100 μg mL^{-1} streptomycin sulfate. Cells were kept in a humidified and 5% CO_2 incubator at 37 °C.

Animals: Nude mice (18–20 g) were purchased from Shanghai Experimental Animal Center (Shanghai). All the animal procedures were performed under the guideline approved by the Institutional Animal Care and Use Committee (IACUC) of the Shanghai Institute of Materia Medica, Chinese Academy of Sciences (CAS).

In Vitro Migration and Invasion: For cell migration assay, MDA-MB-231 cells pre-treated with FeMn-GO at various Fe concentrations for 24 h were harvested and suspended in serum-free medium. Then cell suspensions (0.1 mL, 2×10^4cells) were added into the upper transwell chambers (Corning, USA), and complete media (0.5 mL, 10% FBS) were added into the lower chambers as chemo-attractants. After incubations for 18 h, cells in the upper transwells were removed by cotton swabs. Cells that migrated through the membranes to the lower surface of transwells were fixed with 90% ethanol, stained with crystal violet, and photographed using a microscope. For quantitative analysis, cells were counted in six predetermined 200× fields. Cell invasion assay was performed with 1×10^5 cells per well using the transwell chambers pre-coated with Matrigel (BDBiosciences).

Wound Healing Assay: The wound healing assay was performed as previously described. Briefly, MDA-MB-231cells were pre-treated with FeMn-GO ([Fe] = 10, 20, and 30 μg mL^{-1}) at 37 °C for 24 h. Scratch wounds were made using a 10 μL pipette tip, and cells were washed with PBS for three times. Afterwards, images were captured at the beginning and at 24 h post scratching.

Capillary Tube Formation Assay: The tube formation assay was conducted to evaluate the in vitro anti-angiogenesis effect of FeMn-GO. Briefly, HMEC cells were plated into a 96-well plate pre-coated with 50 μL of Matrigel (BD Biosciences) per well at a density of 2×10^4 cells per well. Meanwhile, varied concentrations of FeMn-GO (10, 20, and 30 μg mL^{-1}) were added into the culture medium. After co-incubations for 8 h, the enclosed networks of capillary tubes were visualized and counted under a microscope in three 200 × fields.

Western Blotting: For Western blotting assay, MDA-MB-231 cells treated with FeMn-GO ([Fe] = 10, 20, and 30 μg mL^{-1}) for 24 h were harvested in RIPA lysis buffer containing 1 mM PMSF. Proteins from cell lysates were separated by a 10% SDS-PAGE and transferred to a nitrocellulose membrane (Invitrogen, USA), blocked with 5% non-fat milk in 0.1% Tween-20/TBS, and blotted with several primary antibodies for matrix metalloproteinase (MMP)-2 (1:1000), α-tubulin (1:2000, Epitomics, USA), urokinase-type plasminogen activator (uPA, 1:400), and Snail (1:400, Santa Cruz Biotechnology, USA).

In Vivo Tissue Compatibility Assay of FeMn-GO: Nude mice (18–20 g) were randomly divided into 4 groups and injected through the tail vein with saline control and FeMn-GO saline solutions with different doses ([Fe] = 2.5, 5, and 10 mg kg^{-1}). The behaviors of mice were monitored every day. After 15 and 30 days of feeding, the mice were sacrificed, and the main organs (heart, liver, spleen, lung and kidney) were removed and stained with hematoxylin-eosin (HE) for histopathological analysis under the optical microscope observation.

In Vitro Cell Viability Assay: In order to determine the in vitro cytotoxicity of FeMn-GO, MDA-MB-231 or HMEC cells were seeded at a density of 5×10^3 cells per well in 96-well culture plates for 12 h. Then the media were changed with fresh ones containing FeMn-GO at various concentrations ranged from 1.25 to 100 μg mL^{-1}. Cells without any treatment were used as control. After co-incubations for 24 or 48 h, cell viability was determined by the sulforhodamine B staining assay using a microplate reader (PerkinElmerEnSpire, USA) at the absorbance wavelength of 565 nm. Each group was repeated in sixtuple. The cytotoxicity was expressed as the percentage of cell viability of treated cells compared with control cells.

Cytotoxicity of Free DOX and DOX-Loaded FeMn-GO Against MCF-7/ADR Cancer Cells: MCF-7/ADR cells were seeded in a 96-well plate with the density of 5×10^3 per well, which was cultured for another 24 h. The cell culture media was substituted with free DOX and DOX-loaded FeMn-GO cell culture solution with the DOX concentrations of 0, 1.25, 2.5, 5, 10, 20, and 30 μg mL^{-1}, respectively. After co-culture for 24 h and 48 h, the culture media was replaced with 100 μL of MTT DMSO solutions (0.8 mg mL^{-1}) and culture for another 4 h. The MTT solution was further replaced with 100 μL of dimethyl sulfoxide (DMSO) per well, and the absorbance was recorded by a microplate reader (Bio-TekELx800) at the wavelength of 490 nm. The cytotoxicity was expressed as the percentage of cell viability compared to untreated control cells.

CLSM Observation of Intracellular Release of DOX from DOX-Loaded FeMn-GO within MCF-7/ADR: MCF-7/ADR cells were seeded into a CLSM-specific culture dish. When the cell density reached 60–80%, the cell culture was replaced with a RPMI 1640 cell culture media with DOX-loaded FeMn-GO dispersions ([DOX] = 10 μg mL^{-1}). After the co-incubation for 4 h, the cells were washed with PBS for three times and the nuclei was stained with DAPI. The fluorescent images were acquired by a CLSM (FV 1000, Olympus, Japan). Three dimensional fluorescence reconstructions of FeMn-GO-endocytosized cells were conducted by

serial layer scanning of cells along Z-axis and 3-D reconstruction of scanned fluorescence images.

Characterizations: Scanning electron microscopy (SEM), scanning transmission electron microscopy (STEM) and EDS spectra were acquired on a field-emission Magellan 400 microscope (FEI Company). Transmission electron microscopy (TEM) was obtained on a JEM-2100F electron microscope operated at 200 kV. The confocal laser scanning microscopy images were recorded in FV1000, Olympus Company. Dynamic light scattering (DLS) were measured on Zetasizer Nanoseries (Nano ZS90). UV-Vis spectra were recorded on a UV-3101PC Shimadzu spectroscope. X-ray photoelectron spectroscopy was recorded on a ESCAlab250, Thermal Scientific. X-ray diffraction (XRD) pattern was collected using a RigakuD/Max-2200 PC X-ray diffractometer with Cu target (40 kV, 40 mA). Fourier transform infrared (FTIR) spectra were obtained in the range of 400–4000 cm^{-1} using a Nicolet 7000-C by dispersing the powder samples in KBr pellets. Thermogravimetry (TG) curves were recorded on a Netzsch STA449C microanalyzer in air flow at 10 K min^{-1}.

Acknowledgements

This work was supported by the National Nature Science Foundation of China (Grant No. 51302293, 51132009, 51072212, 81270047, 21177137), the National Basic Research Program of China (973 Program, Grant No. 2011CB707905, 2010CB934000), China National Funds for Distinguished Young Scientists (Grant No.51225202), Natural Science Foundation of Shanghai (13ZR1463500), Nano Special Program of the Science and Technology Commission of Shanghai (Grant No. 11nm0506500) and Foundation for Youth Scholar of State Key Laboratory of High Performance Ceramics and Superfine Microstructures (Grant No. SKL201203). Y.C. and P.X. contributed equally to this manuscript.

Received: January 21, 2014
Revised: February 9, 2014
Published online: April 1, 2014

[1] a) D. Peer, J. M. Karp, S. Hong, O. C. FaroKhzad, R. Margalit, R. Langer, *Nat. Nanotechnol.* **2007**, *2*, 751; b) V. Wagner, A. Dullaart, A. K. Bock, A. Zweck, *Nat. Biotechnol.* **2006**, *24*, 1211–1217; c) Y. Chen, H. Chen, J. Shi, *Adv. Mater.* **2013**, *25*, 3144.

[2] a) M. A. C. Stuart, W. T. S. Huck, J. Genzer, M. Muller, C. Ober, M. Stamm, G. B. Sukhorukov, I. Szleifer, V. V. Tsukruk, M. Urban, F. Winnik, S. Zauscher, I. Luzinov, S. Minko, *Nat. Mater.* **2010**, *9*, 101; b) J. L. Vivero-Escoto, Slowing II, B. G. Trewyn, V. S. Y. Lin, *Small* **2010**, *6*, 1952.

[3] a) M. S. Yavuz, Y. Y. Cheng, J. Y. Chen, C. M. Cobley, Q. Zhang, M. Rycenga, J. W. Xie, C. Kim, K. H. Song, A. G. Schwartz, L. H. V. Wang, Y. N. Xia, *Nat. Mater.* **2009**, *8*, 935; b) Y. F. Zhu, J. L. Shi, W. H. Shen, X. P. Dong, J. W. Feng, M. L. Ruan, Y. S. Li, *Angew. Chem. Int. Ed.* **2005**, *44*, 5083.

[4] a) Y. Chen, Q. Yin, X. F. Ji, S. J. Zhang, H. R. Chen, Y. Y. Zheng, Y. Sun, H. Y. Qu, Z. Wang, Y. P. Li, X. Wang, K. Zhang, L. L. Zhang, J. L. Shi, *Biomaterials* **2012**, *33*, 7126; b) Y. Zhou, Z. Wang, Y. Chen, H. Shen, Z. Luo, A. Li, Q. Wang, H. Ran, P. Li, W. Song, Z. Yang, H. Chen, Z. Wang, G. Lu, Y. Zheng, *Adv. Mater.* **2013**, *25*, 4123; c) M. F. Bennewitz, T. L. Lobo, M. K. Nkansah, G. Ulas, G. W. Brudvig, E. M. Shapiro, *ACS Nano* **2011**, *5*, 3438–3446; d) S. H. Crayton, A. Tsourkas, *ACS Nano* **2011**, *5*, 9592.

[5] a) Z. Liu, J. T. Robinson, X. M. Sun, H. J. Dai, *J. Am. Chem. Soc.* **2008**, *130*, 10876; b) K. Yang, L. Z. Feng, X. Z. Shi, Z. Liu, *Chem. Soc. Rev.* **2013**, *42*, 530; c) K. Yang, Y. J. Li, X. F. Tan, R. Peng, Z. Liu, *Small* **2013**, *9*, 1492.

[6] a) L. M. Zhang, Z. X. Lu, Q. H. Zhao, J. Huang, H. Shen, Z. J. Zhang, *Small* **2011**, *7*, 460; b) H. Q. Bao, Y. Z. Pan, Y. Ping, N. G. Sahoo, T. F. Wu, L. Li, J. Li, L. H. Gan, *Small* **2011**, *7*, 1569.

[7] a) C. S. Wang, J. Y. Li, C. Amatore, Y. Chen, H. Jiang, X. M. Wang, *Angew. Chem. Int. Ed.* **2011**, *50*, 11644; b) S. H. Hu, Y. W. Chen, W. T. Hung, I. W. Chen, S. Y. Chen, *Adv. Mater.* **2012**, *24*, 1748; c) G. Gollavelli, Y. C. Ling, *Biomaterials* **2012**, *33*, 2532.

[8] a) Y. Wang, Y. Y. Shao, D. W. Matson, J. H. Li, Y. H. Lin, *ACS Nano* **2010**, *4*, 1790; b) M. Pumera, *Mater. Today* **2011**, *14*, 308.

[9] a) K. Yang, S. A. Zhang, G. X. Zhang, X. M. Sun, S. T. Lee, Z. A. Liu, *Nano Lett.* **2010**, *10*, 3318; b) J. T. Robinson, S. M. Tabakman, Y. Y. Liang, H. L. Wang, H. S. Casalongue, D. Vinh, H. J. Dai, *J. Am. Chem. Soc.* **2011**, *133*, 6825; c) B. Tian, C. Wang, S. Zhang, L. Z. Feng, Z. Liu, *ACS Nano* **2011**, *5*, 7000; d) K. Yang, L. L. Hu, X. X. Ma, S. Q. Ye, L. Cheng, X. Z. Shi, C. H. Li, Y. G. Li, Z. Liu, *Adv. Mater.* **2012**, *24*, 1868; e) M. Li, X. J. Yang, J. S. Ren, K. G. Qu, X. G. Qu, *Adv. Mater.* **2012**, *24*, 1722.

[10] Y. H. Xue, H. Chen, D. S. Yu, S. Y. Wang, M. Yardeni, Q. B. Dai, M. M. Guo, Y. Liu, F. Lu, J. Qu, L. M. Dai, *Chem. Commun.* **2011**, *47*, 11689.

[11] X. J. Fan, G. Z. Jiao, W. Zhao, P. F. Jin, X. Li, *Nanoscale* **2013**, *5*, 1143.

[12] a) J. Perez-Rodriguez, S. Lai, B. D. Ehst, D. M. Fine, D. A. Bluemke, *Radiology* **2009**, *250*, 371; b) Y. Chen, H. Chen, S. Zhang, F. Chen, S. Sun, Q. He, M. Ma, X. Wang, H. Wu, L. Zhang, L. Zhang, J. Shi, *Biomaterials* **2012**, *33*, 2388.

[13] H. B. Na, J. H. Lee, K. J. An, Y. I. Park, M. Park, I. S. Lee, D. H. Nam, S. T. Kim, S. H. Kim, S. W. Kim, K. H. Lim, K. S. Kim, S. O. Kim, T. Hyeon, *Angew. Chem. Int. Ed.* **2007**, *46*, 5397.

[14] M. H. Lee, Z. Yang, C. W. Lim, Y. H. Lee, S. Dongbang, C. Kang, J. S. Kim, *Chem. Rev.* **2013**, *113*, 5071.

[15] H. S. Choi, W. Liu, P. Misra, E. Tanaka, J. P. Zimmer, B. I. Ipe, M. G. Bawendi, J. V. Frangioni, *Nat. Biotechnol.* **2007**, *25*, 1165.

[16] Z. Liu, X. M. Sun, N. Nakayama-Ratchford, H. J. Dai, *ACS Nano* **2007**, *1*, 50.

[17] L. Y. Feng, L. Wu, X. G. Qu, *Adv. Mater.* **2013**, *25*, 168.

[18] P. Xu, Q. Yin, J. Shen, L. Chen, H. Yu, Z. Zhang, Y. Li, *Int. J. Pharm.* **2013**, *454*, 21–30.

[19] a) S. G. Kang, G. Q. Zhou, P. Yang, Y. Liu, B. Y. Sun, T. Huynh, H. Meng, L. N. Zhao, G. M. Xing, C. Y. Chen, Y. L. Zhao, R. H. Zhou, *Proc. Natl. Acad. Sci. U.S.A.* **2012**, *109*, 15431; b) H. Meng, G. M. Xing, E. Blanco, Y. Song, L. N. Zhao, B. Y. Sun, X. D. Li, P. C. Wang, A. Korotcov, W. Li, X. J. Liang, C. Y. Chen, H. Yuan, F. Zhao, Z. Chen, T. Sun, Z. F. Chai, M. Ferrari, Y. L. Zhao, *Nanomed. Nanotechnol.* **2012**, *8*, 136–146.

[20] Y. Gao, Y. Chen, X. F. Ji, X. Y. He, Q. Yin, Z. W. Zhang, J. L. Shi, Y. P. Li, *ACS Nano* **2011**, *5*, 9788.